Journal of
MATERIALS RESEARCH

Article
DOI:10.1557/s43578-023-01181-9

Structural, elastic, optoelectronic, and transport properties of Na-based halide double perovskites Na_2CuMX_6 (M = Sb, Bi, and X = Cl, Br) as renewable energy materials: A DFT insight

Ahmad Ayyaz[1,a], **G. Murtaza**[1,a], **M. Umer**[2], **Ahmad Usman**[1], **Hafiz Hamid Raza**[1]

[1] *Centre for Advanced Studies in Physics, GC University, Lahore, Pakistan*
[2] *Institute of Chemical Sciences, GC University, Lahore, Pakistan*
[a] Address all correspondence to these authors. e-mails: raiayyaz23@gmail.com; gmrai@gcu.edu.pk

Received: 3 August 2023; accepted: 27 September 2023; published online: 4 October 2023

The structural, elastic, optoelectronic, and transport properties of the double perovskites Na_2CuMX_6 (M = Sb, Bi, and X = Cl, Br) were investigated through the utilization of the DFT-based WIEN2k and BoltzTraP codes. We first explored the structural, electrical, and optical characteristics of Na_2CuMX_6 using the generalized gradient approximations (GGA) and the GGA modified by the Tran-Balaha modified Becke-Johnson exchange potential (GGA + mBJ). The stability of structures was ensured by the tolerance factor. The mechanical stability was verified by employing Born Criteria, whereas estimated negative formation energy and Gibbs free energy confirmed thermodynamic stability. The indirect electronic bandgap nature was validated for all perovskites by computing electronic band structures. The absorption spectrum and other calculated optical parameters of Na_2CuMX_6 between 1.7 and 3.4 eV hold notable importance in applications involving solar cells. The BoltzTraP code was utilized to execute the transport property calculations. The computational observations presented in this study hold significant value for future renewable energy applications.

Introduction

The remarkable physical properties and possible applications of lead-free halide perovskites have inspired many researchers. Perovskites are employed in numerous optoelectronic devices, including solar cells. These materials have important optoelectronic properties, such as strong optical absorption, carrier mobility, charge diffusion, residual point defects, an adjustable band gap, and a small effective mass of the carriers. Additionally, these inexpensive materials are widely available, promoting research into them to build affordable solar cells rather than depending on costly Si materials [1, 2]. Regardless of several exceptional qualities, lead halide perovskites have two major challenges that significantly limit their effectiveness in applications: the toxicity brought on by the presence of lead and material instability under ambient circumstances [3–5]. Therefore, the creation of lead-free perovskites presents a useful and efficient means of overcoming these limitations [6–11]. Typically, toxic-free metal halide perovskites have low reflectivity, high optical conductivity, and high absorptivity, making them suitable for commercial utilization in solar cells, thermoelectric, and optoelectronic devices [12]. One of the most effective ways to get lead-free perovskites is the process of exchanging two Pb^{2+} cations for two metal cations, with one being monovalent [M (I)] and the other being trivalent [M (III)]. This substitution produces the $A_2M(I)M(III)X_6$ perovskites, which contain a stable cubic structure [13]. Bi- and Sb-based perovskites such as Na_2CuMCl_6 (M = Bi, Sb), Na_2AgSbX_6 (F, Cl, Br, I), and Cs_2CuMCl_6 (M = Bi, Sb) have attracted the most interest within this group of materials because of their increased stability, distinctive electronic properties, and photoluminescence [13–15]. DFT-based theoretical studies have recently indicated that the cubic crystal structure of lead-free double perovskites exhibits greater stability compared to the hexagonal structure. [16].

Numerous DFT computations have been carried out as a consequence of improvements in computing techniques and the expanding accessibility of computational facilities. Structure prediction is a rapidly expanding area of research as a result of the addition of increasingly sophisticated and accurate minimization techniques to DFT [17]. DFT has been used in computational methods to explain a lot about the chemical and physical properties of organic, inorganic, and hybrid perovskites [18]. Tang et al. investigated the variation in optical properties of A_2CuSbX_6 (A = Cs, Rb, and K; X = Cl, Br) and concluded that $K_2CuSbCl_6$ is a potential candidate for solar cells [19]. Kumari, Sunita, et al. computed the optical and thermoelectric features of Na_2AgSbX_6 (F, Cl, Br, and I) for their utilization in thermoelectric and photovoltaic devices [15]. The applications of Rb_2ScAgX_6 (X = Cl, Br, and I) materials in PV cells and thermoelectric generators have also been discussed by Asghar et al. [20]. Most recently, the physical features of Cs_2GeSnX_6 (X = Cl, Br) were investigated employing DFT analysis for their potential applications in photovoltaics [21].

In this context, we examined the structural, elastic, optoelectronic, and transport characteristics using WIEN2K and BoltzTraP codes according to the perspective of the available literature. The outline of this study is: "Introduction" section provides a broad introduction, whereas "Results and discussion" section includes the results. The overall conclusion of this work is covered in "Conclusion" and "Computational details" sections provides computation details. Future studies into the disciplines of solar cells and thermoelectric generators will be contributed by our results for applications in renewable energy.

Results and discussion

Structural properties

The materials Na_2CuMX_6 (M = Sb, Bi, and X = Cl, Br) exhibit a cubic structure belonging to the space group Fm-3 m (#225). One of these families of double perovskite compounds, Na_2CuMX_6, exhibits sp^3–d^2 hybridization and in this structure, the cations Cu^{1+} and M^{3+} occupy alternating positions, forming a rock salt superstructure [22]. Halide double perovskites are known to have this rock-salt superstructure phase as their ground state [23]. Six halide ions ($Cl^-$and Br^-) surround the Cu^{1+} and M^{3+} (Sb^{3+} and Bi^{3+}) cations in the center of the octahedral to form CuX_6 and MX_6 octahedral complexes, respectively. Figure 1(a) depicts the arrangement of these substances in a crystalline structure, where they form octahedral complexes that share corners with the Cs cation positioned at the center of the cuboctahedral [24]. The Location of the Na atom in the unit cell is (3/4, 1/4, 1/4), the Cu atom is at (0, 0, 0,), the M (Sb and Bi) atom is at (1/2, 0, 0), and the X (Br and Cl) anion is at (3/4, 0, 0). Goldschmidt's tolerance factor is employed to investigate the structural stability or degree of distortion of all compounds using the following expression [25].

$$\tau = \frac{r_{Na} + r_X}{\sqrt{2}(\frac{r_{Cu}+r_M}{2} + r_X)} \tag{1}$$

Here, r_{Na}, r_{Cu}, r_M, and r_X represent the corresponding atomic radii of the Na, Cu, M (Sb and Bi), and X (Cl and Br) atoms. Fedorovskiy et al. reported that a tolerance factor of $0.7 \ll 1.2$ is allowed to generate stable crystal structures [26]. Therefore, all the compounds have stable cubic structures whose values lie within the allowed range (see Table 1). We also computed the formation energy to evaluate the stability of the material. To estimate the formation energy, we utilized the expression [27]:

$$E_f = E_{Na2CuMX6} - (2E_{Na} + E_{Cu} + E_M + 6E_X) \tag{2}$$

Here $E_{Na2CuMX6}$ is the total energy of Na_2CuMX_6 (M = Sb, Bi, and X = Cl, Br) compounds, and the E_{Na}, E_{Cu}, E_M, and E_X are the energies of the atoms individually. The confirmation of the thermodynamic stability of the double perovskites being investigated is evidenced by the presence of negative values for their formation energy, as depicted in Table 1 [28]. Furthermore, thermodynamic stability can be investigated through the computation of Gibbs free energy using the GIBBS2 computational mode [29]. The estimated Gibbs free energy (G) values were -2.95×10^7 kJ/mol, -6.33×10^7 kJ/mol, -6.91×10^7 kJ/mol, and -1.03×10^7 kJ/mol for $Na_2CuSbCl_6$, $Na_2CuSbBr_6$, $Na_2CuBiCl_6$, and $Na_2CuBiBr_6$, respectively. These negative results once again provide evidence of the thermodynamic stability of both double perovskites.

The structural parameters such as equilibrium lattice parameter, bulk modulus (B), bulk modulus derivative (B'), volume at ground state (V_0), and ground state energy (E_0) are optimized by implementing the Murnaghan equation of state [30]:

$$E(V) = E_0(V) + \left[\frac{B_0 V}{B'_0(B'_0 - 1)}\right] \times \left[B_0\left(1 - \frac{V_0}{V}\right) + \left(\frac{V_0}{V}\right)^{B'_0} - 1\right] \tag{3}$$

Here V_0 is the ground state volume of the unit cell, B represents Bulk modulus, and $B\prime$ is the pressure associated with unit cell volume. With the use of a volume optimization procedure for each compound as shown in Fig. 1(b–e), the total energy is changed against the volume of the unit cell, and by putting in the equation, structural parameters (a, B, B',E_0 and V0) are determined as shown in Table 1.

Elastic properties

The mechanical stability was evaluated by measuring mechanical properties such anisotropy (A), shear modulus (G), bulk modulus (B), and second-order elastic constants (C_{ij}). The elastic constants C_{11}, C_{12}, and C_{44} govern the dimensional structural strength of cubic perovskite materials. Where C_{11} represents material resistance to strain, C_{12} represents shear stress, and C_{44} represents resistance to shear deformation

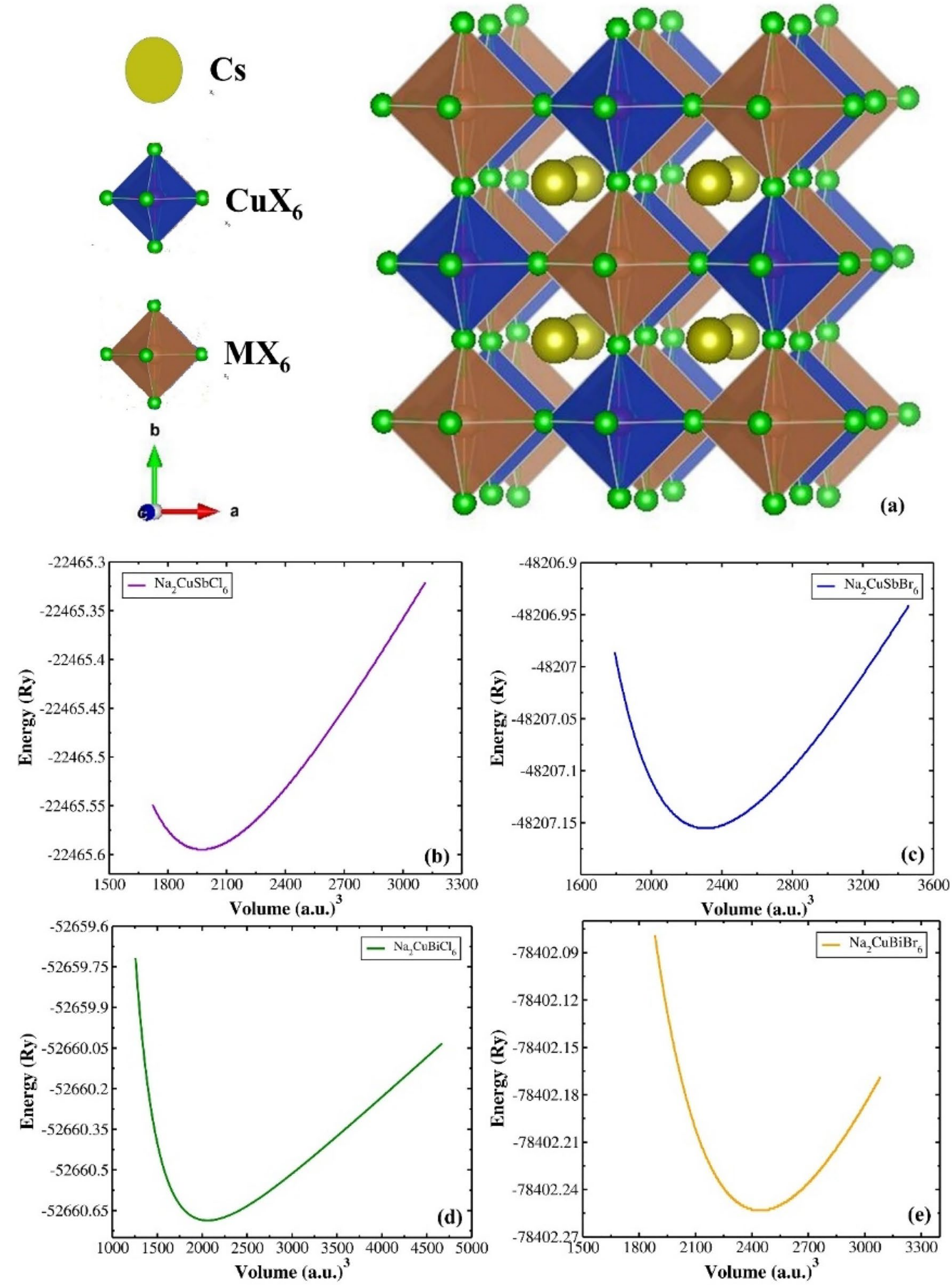

Figure 1: (a) The rock salt structure (b–e) the volume optimization against energy of Na_2CuMX_6 (M = Sb, Bi, and X = Cl, Br).

[21, 31]. The Born-Huang stability criteria, which is $C_{11} > 0$, $C_{12} > 0$, $C_{44} > 0$, $C_{11} + 2C_{12} > 0$, and $C_{11}–C_{12} > 0$, is used to determine the structural stability of $Na_2CuSbCl_6$, $Na_2CuSbBr_6$, $Na_2CuBiCl_6$, and $Na_2CuBiBr_6$ [32]. This leads us to conclude that the mechanical stability of halide-double perovskite material structures is high. The two models used to calculate shear

TABLE 1: The parameters of Na_2CuMX_6 (M = Sb, Bi, and X = Cl, Br) obtained by utilizing PBE-GGA.

Parameter	$Na_2CuSbCl_6$	$Na_2CuSbBr_6$	$Na_2CuBiCl_6$	$Na_2CuBiBr_6$
a = b = c (Å)	10.53	11.12	10.75	11.05
B_0 (GPa)	30.49	24.02	25.13	22.99
B'	5.94	5.54	5.70	5.0
V_0 (a.u.)^3	1972.77	2306.34	2060.55	2442.89
E_0 (Ry)	− 22465.72	− 48207.15	− 52660.15	− 78402.25
τ	0.82	0.82	0.78	0.78
E_f (eV/atom)	− 2.404	− 1.98	− 2.68	− 2.28

modulus Voigt's (GV) and Reuss' (GR), were used to measure a material's resistance to reversible deformation. Hill G_H, on the other hand, is computed by taking the arithmetic mean of G_V and G_R [33]:

$$G_H = \frac{(G_V + G_R)}{2} \tag{4}$$

The determination of Young's modulus is often used to determine the response of a crystalline substance to a linear deformation, and bulk modulus was obtained by using the following formula [34]:

$$Y = \frac{9BG_V}{3B + G_V} \tag{5}$$

$$B = \frac{C_{11} + 2C_{12}}{3} \tag{6}$$

The capacity to withstand variations in volume during compression is determined by Bulk modulus (B) of materials. Strong crystals are indicated by high B values, whereas resistance to deformation from plasticity is measured by shear modulus (G). The values of B determined for compounds $Na_2CuBiCl_6$ and $Na_2CuBiBr_6$ are 10.72 GPa and 10.32 GPa, respectively, while those for $Na_2CuSbCl_6$ and $Na_2CuSbBr_6$ are 10.293 GPa and 8.438. Cl-based compounds are more resistant to volume change than Br-based compounds due to their greater B value, and similarly, Cl-based compounds that have a high G value have high resistance to transverse bending. The Pugh's ratio (B/G) can be used to reveal ductility or brittleness [35]. Materials with a B/G value beyond 1.75 are classified as ductile, whilst those exhibiting a value below 1.75 are categorized as brittle [36]. The calculated B/G values for all compounds show a brittle nature except $Na_2CuSbCl_6$, which exhibits ductile nature. Poisson's ratio (υ) is another parameter that differentiates between the brittle and ductile behavior of materials. A ductile compound has a Poisson's ratio (υ) larger than 0.26, whereas a brittle one has a value less than 0.26 [37]. All of the anticipated values of υ for the compounds indicate that the materials are brittle except for $Na_2CuSbCl_6$, which reveals a ductile nature. Furthermore, an anisotropy factor (A) has been calculated, with unity representing isotropic behavior and deviations from this value representing anisotropic behavior [38, 39]. All calculated values shown in the table indicate that all compounds are anisotropic. Cauchy's pressure, calculated from $C_p = C_{12}–C_{44}$ was used to derive information about the type of bonding. Cp values that are positive signify ionic nature, whereas negative value denotes covalent bonding [40]. The negative values of C_p reveal the covalent nature of materials. Another term is shear constant C′ which gives information about the stability of a compound if C′ >0, and its formula is:

$$C\prime = \frac{(C_{11} - C_{12})}{2} \tag{7}$$

Based on the estimated values, it can be determined that all substances exhibit dynamic stability. In addition, we investigated Debye temperature, which is related to elastic properties calculated as [41]:

$$\theta_D = \frac{h}{K_B}\left[\frac{3n}{4\pi}\left(\frac{N_A\rho}{M}\right)\right]^{-1/3} V_m \tag{8}$$

Elastic anisotropy

Materials anisotropy is essential for understanding their mechanical strength and estimating microhardness. The formation of cracks at the micro level in the compounds might be caused by a considerable elastic anisotropy [42]. Using the ELATE program, contour graphs in three dimensions have been generated for further analyzing the elastic anisotropy of crystals through their respective moduli [43]. For Na_2CuMX_6 (M = Sb, Bi, and X = Cl, Br), double perovskite materials, elastic modulus graphs involving linear compressibility (β), Young's modulus (Y), shear modulus (G), and Poisson's ratio (υ), are obtained from the computed C_{ij} and shown in Figs. 2 and 3. Isotropic elastic behavior does not always manifest in cubic crystals. The Zener anisotropic factor (A) is a measure of the degree of elastic anisotropy of the material. When A = 1, a crystal is said to be entirely isotropic, and variations in the given value indicate the presence of elastic anisotropy [39]. Elastic anisotropy (A) is determined for cubic crystals as follows [44]:

$$A = \frac{2C_{44}}{C_{11} - C_{12}} \tag{9}$$

In addition, the maximum ranges are shown by the blue curves in Figs. 2 and 3, while the lowest values are represented by the green curves for linear compressibility (β), Young's modulus (Y), and shear modulus (G). Whereas, for Poisson's ratio, maximum ranges are represented by blue and minimum values by red curves.

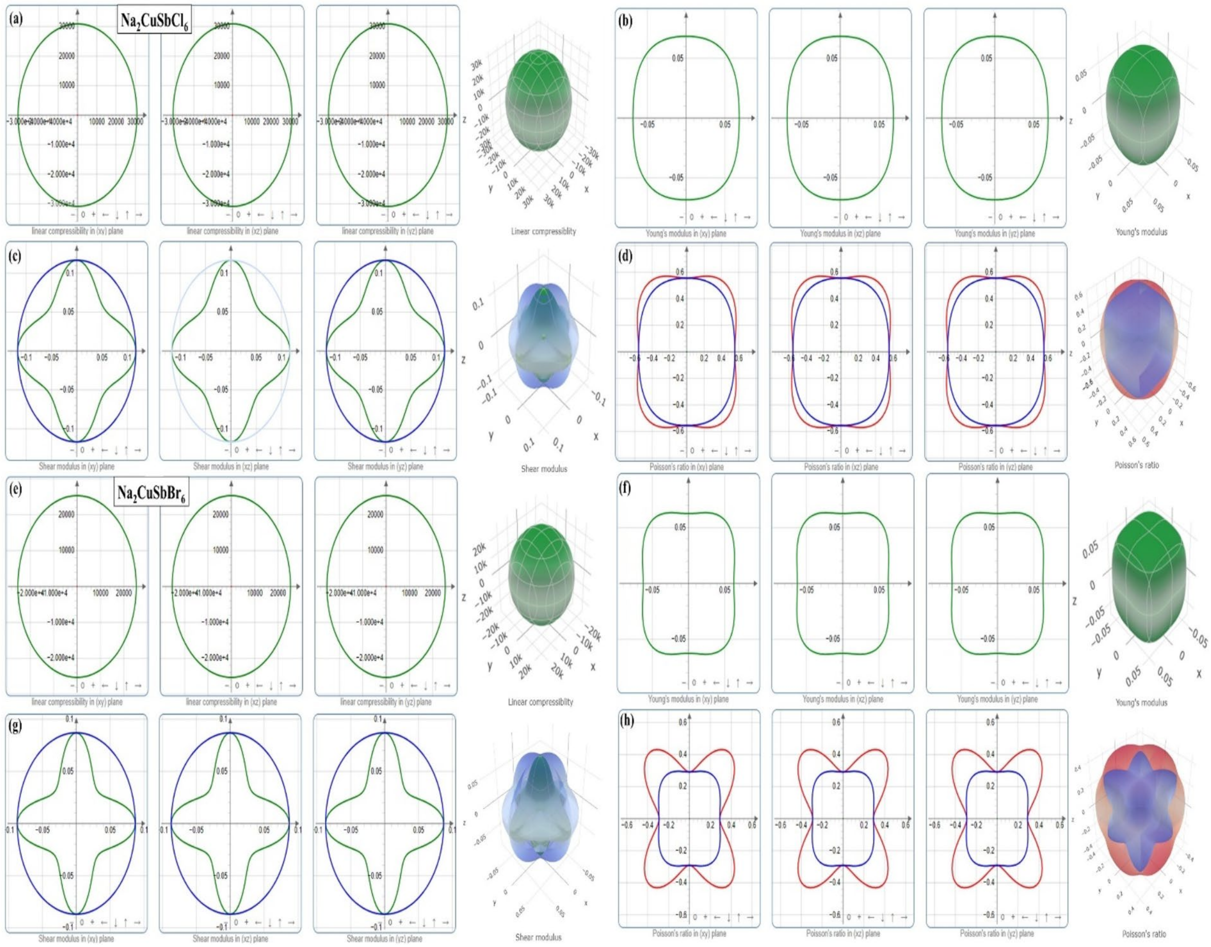

Figure 2: A three-dimensional illustration of linear compressibility, Young's modulus, shear modulus, and Poisson's ratio for (a–d) $Na_2CuSbCl_6$ (e, f) $Na_2CuSbBr_6$.

The results suggest that the linear compressibility, as seen in Figs. 2 and 3, exhibits isotropic properties when the value of A is equal to one, as indicated in Table 2. In contrast, it can be shown that Young's modulus, Shear modulus, and Poisson's ratio (υ) exhibit anisotropic characteristics across all compounds that have been investigated. The depiction of Young's modulus illustrates that $Na_2CuBiBr_6$ exhibits the highest level of anisotropy compared to $Na_2CuSbCl_6$, $Na_2CuSbBr_6$, and $Na_2CuBiCl_6$. The shear modulus follows the same trend as that for Young's modulus. Furthermore, the Poisson's ratio shows the sequence: $Na_2CuBiCl_6 > Na_2CuBiBr_6 > Na_2CuBiCl_6 > Na_2CuBiBr_6$. Table 2 presents the values of elastic moduli together with their corresponding anisotropy values.

Electronic properties

The material's electronic characteristics dictate how well it may be used in different optoelectronic devices. The Trans–Blaha modified Becke–Johnson (TB-mBJ) potential is used to figure out the energy band structure, total density of states (TDOS), and partial density of states (PDOS) to describe the electronic properties [32]. The current study uses PBE-GGA, PBEsol-GGA, and mBJ to identify the band structures of Na_2CuMX_6 (M = Sb, Bi, and X = Cl, Br) while considering the optimized unit cell. Figure 4 depicts the calculated band structures across the Fermi energy level in the Brillouin zone along the high-symmetry path W → L → Γ → X → W → K with energies between − 4 eV and 8 eV. The band structures of $Na_2CuSbCl_6$ and $Na_2CuSbBr_6$ as determined by the PBE-GGA, PBEsol-GGA, and TB-mBJ functionals are shown in Fig. 4(a–f). The X-point was determined as the location of the valence band maximum (VBM), while the L-point was identified as the position of the conduction band minimum (CBM) revealing an indirect band gap for all compounds. The bandgap computed by PBE-GGA for $Na_2CuSbCl_6$ and $Na_2CuSbBr_6$ was 0.83 eV and 0.6 eV, respectively. By employing PBEsol-GGA, the band gap was found to be 0.79 eV and 0.56 eV for both compounds. The indirect band gaps were improved to 1.26 eV for $Na_2CuSbCl_6$ and 1.3 eV for

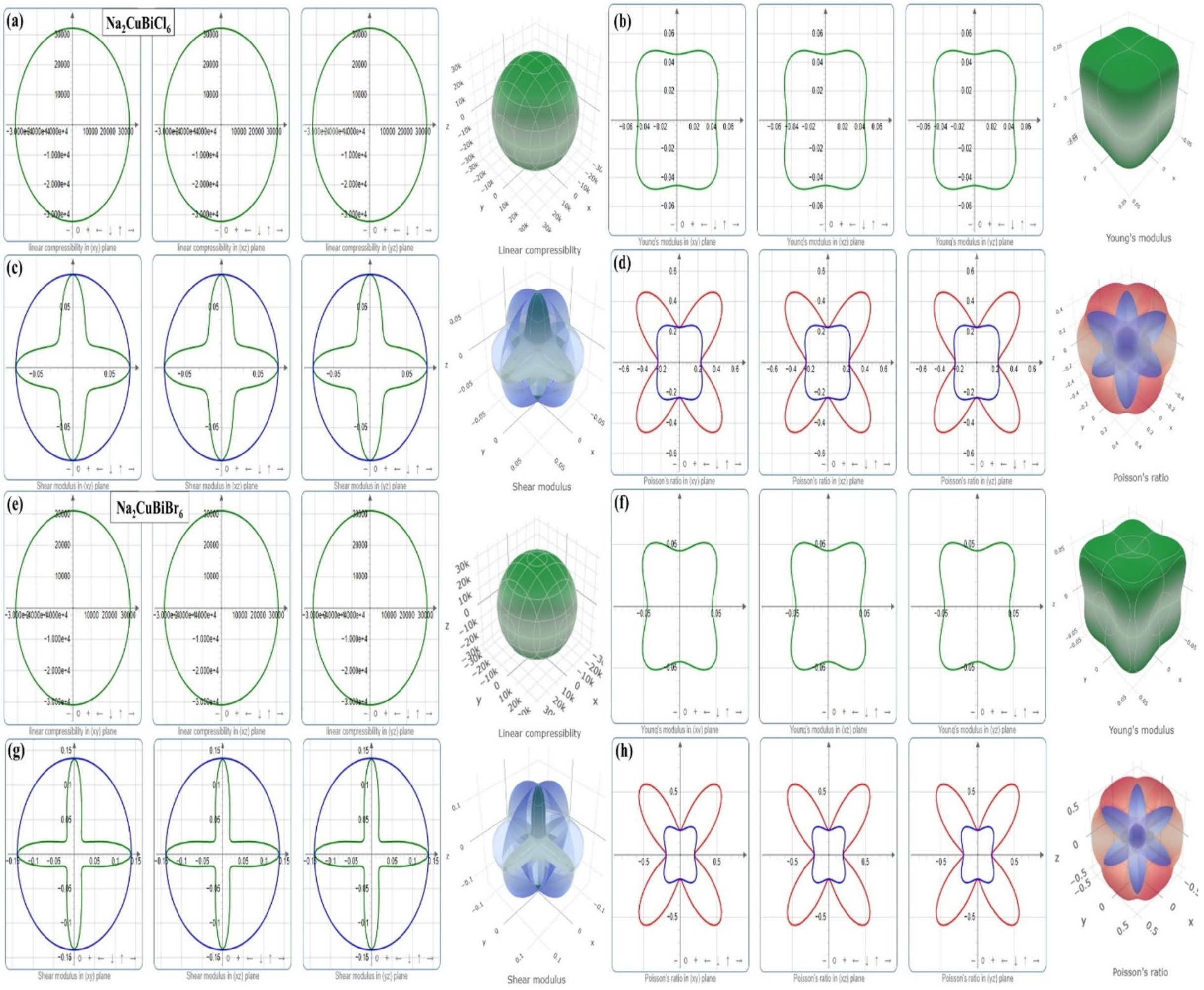

Figure 3: A three-dimensional illustration of linear compressibility, Young's modulus, shear modulus, and Poisson's ratio for (a–d) $Na_2CuBiCl_6$ (e, f) $Na_2CuBiBr_6$.

$Na_2CuSbCl_6$ when GGA combined with mBJ potential was employed. By shifting the Cu-d and Cl-p dominated energy bands away from the Fermi level, the mBJ-potential broadened the bandgap. Similarly, the comparison between the band structures calculated using PBE-GGA, PBEsol-GGA, and mBJ for $Na_2CuBiCl_6$ and $Na_2CuBiBr_6$ is presented in Fig. 4(g–l). The band gaps of both materials have indirect nature. Bandstucure plotting reported the band gap (Eg) for $Na_2CuBiCl_6$ is 1.62 eV (L–X) while decreases to 1.57 eV (L–X) for $Na_2CuBiBr_6$ double perovskites using TB-mBJ functional due to increase in atomic radius. The calculated band gaps were slightly higher than the previously reported band gaps of $Na_2CuBiCl_6$ and $Na_2CuSbCl_6$ [14].

Furthermore, the density of states illustrated in Fig. 5(a–d) depicts the distribution of electrons in Na_2CuMX_6 (M = Sb, Bi, and X = Cl, Br), Na, Cu, Sb/Br, and Cl/Br atoms. The DOS plots provide evidence for the band structure as well as the semiconducting characteristics [45]. The DOS plots of compounds under study show identical behavior with band structure. The electrons of the sodium (Na) atom are situated in the inner region, distanced from the valence and conduction bands, which have negligible impact on the transition mechanism. The transitions and recombination of electrons in Cu are primarily influenced by the d-state electrons, while in Sb/Bi and Cl/Br, the electrons in the p-state have a considerable contribution. The maximum contribution in the valence band (VB) and the formation of conduction band (CB) minima are primarily attributed to the presence of 3d-Cu and p-Cl/Br; Consequently, electrons also transition between the halide ions and 3d-Cu states.

To get a comprehensive understanding of the electronic characteristics, an investigation was conducted to estimate the charge density profile within the (110) plane in a cross-section, as shown in Fig. 6. The Pauling electronegativity values of all elements are Na (0.93), Cu (1.90), Sb (2.05), Bi (1.9), Cl (3.16),

TABLE 2: Elastic parameters and variations in elastic moduli of all compounds.

Parameters	$Na_2CuSbCl_6$	$Na_2CuSbBr_6$	$Na_2CuBiCl_6$	$Na_2CuBiBr_6$
C_{11} (GPa)	14.63	15.96	21.96	22.27
C_{12} (GPa)	8.12	4.66	5.09	4.34
C_{44} (GPa)	8.56	11.49	12.91	7.21
B (GPa)	10.29	8.44	10.72	10.32
G (GPa)	5.81	8.65	10.88	7.87
Y (GPa)	15.98	20.18	24.78	18.90
B/G	1.77	0.97	0.98	1.31
υ	0.28	0.13	0.12	0.19
C′ (GPa)	3.25	5.66	8.43	8.97
θ_D (K)	163.1	158.9	202.49	145.6
Linear compressibility (TPa^{-1})				
β_{min}	30880	25314	32149	30951
β_{max}	30880	25314	32149	30951
A	1	1	1	1
Young's modulus (GPa)				
Y_{min}	0.068	0.062	0.045	0.044
Y_{max}	0.076	0.081	0.066	0.077
A	1.1	1.3	1.4	1.7
Shear modulus (GPa)				
G_{min}	0.076	0.044	0.029	0.028
G_{max}	0.12	0.08	0.08	0.13
A	1.5	1.9	2.6	4.9
Poisson's ratio				
υ_{min}	− 0.68	− 0.56	− 0.61	− 0.77
υ_{max}	− 0.55	− 0.29	− 0.23	− 0.19
A	0.8	0.5	0.4	0.25

and Br (2.96). The transition metal Cu, Sb and Bi atoms with Cl and Br atoms have lesser electronegativity differences, which is evidence of covalent bonds like Cu–Cl, Cu–Br, Sb–Cl, Sb–Br, Bi–Cl, and Bi–Br for the respective compounds. While there is ionic bonding between Na and Cl/Br due to their large electronegativity differences. The covalence nature is attributed to hybridization between the Cu-3d and Cl-3p, Cu-3d and Br-4p, Sb-5p and Cl-3p, Sb-5p and Br-4p, Bi-6p and Cl-3p, and Bi-6p and Br-4p state for their respective compounds, according to the PDOS spectra as expressed in Fig. 5.

Optical properties

The band gap, absorption of energy, and efficiency of materials for converting light into electrical power determine the optoelectronic and solar cell properties of materials [46]. The material interaction with light can result in either an intra-band or an inter-band transition; the latter is responsible for excitations and recombination. In optical applications, this transition is valuable [47]. As a result, Fig. 7 shows the optical characteristics of the investigated compounds as estimated within the region of 0–6 eV energy. The optical behavior of Na_2CuMX_6 (M = Sb, Bi, and X = Cl, Br) has been described by the real and imaginary dielectric functions dependent on energy as follows:

$$\varepsilon(\omega) = \varepsilon_1(\omega) + i\varepsilon_2(\omega)$$

Here $\varepsilon_1(\omega)$ specifies the real part of the dielectric function and $\varepsilon_2(\omega)$ denotes the imaginary part of the dielectric function. The $\varepsilon_1(\omega)$ defines a certain amount of polarization within a material when light interacts and the quantity of light lost caused by dispersion is denoted by $\varepsilon_2(\omega)$. This is also expressed concerning the energy that the materials attenuate or absorb [48–53].

The computed real component of the dielectric function $\varepsilon_1(\omega)$ for $Na_2CuSbCl_{6,}$ $Na_2CuSbBr_{6,}$ $Na_2CuBiCl_{6,}$ and $Na_2CuBiBr_6$ are displayed in Fig. 7(a). This component describes the dispersive behavior of the material to incoming photons [54]. The static value of $\varepsilon_1(\omega)$ is highest for $Na_2CuSbBr_6$ (3.44) in comparison to $Na_2CuBiBr_6$ (3.05), $Na_2CuSbCl_6$ (2.88), and $Na_2CuBiCl_6$ (2.45). This value rises as the band gap narrows [55]. Additionally, the values of $\varepsilon_1(\omega)$ are positive throughout the whole energy region, which justifies the fact that none of the Na_2CuMX_6 double perovskites reflects photons in the 0–6 eV range [56]. Furthermore, for the investigated perovskites, the maximum $\varepsilon_1(\omega)$ values lie inside the visible region. This confirms that these substances respond to the visible spectrum most strongly.

The relationship between the value of $\varepsilon_2(\omega)$ and the energy is illustrated in Fig. 7(b). The $\varepsilon_2(\omega)$ represents the optical band gap and absorption properties [57]. There is no evidence of absorption up to 1.2 eV, 1.4 eV, 1.6 eV, and 1.7 eV for $Na_2CuSbCl_{6,}$ $Na_2CuSbBr_{6,}$ $Na_2CuBiCl_{6,}$ and $Na_2CuBiBr_6$, respectively, proving that the predicted electrical bandgap and optical bandgap are almost identical.

The refractive index n(ω) represents the process in which light propagates through the materials under investigation [58]. The static refractive indices, n(0), for the spectra of $Na_2CuSbCl_{6,}$ $Na_2CuSbBr_{6,}$ $Na_2CuBiCl_{6,}$ and $Na_2CuBiBr_6$ are 1.7, 1.85, 1.56, and 1.75**.** The peak values of $n(\omega)$ are 2.14, 2.25, 1.87, and 2.05 for $Na_2CuSbCl_{6,}$ $Na_2CuSbBr_{6,}$ $Na_2CuBiCl_{6,}$ and $Na_2CuBiBr_6$, respectively, in the 1.7–2.0 eV photon energy range, as shown in Fig. 7(c). The same patterns of graphs with increased energy are shown by the correspondence between $\varepsilon_1(\omega)$ and n(ω), which is essential for the validity of the findings. Additionally, the decay of light energy is indicated by the extinction coefficient k(ω), which is illustrated as an imaginary part of the refraction of light [46]. The values of k(ω) depicted in Fig. 7(d) consolidate with the values of $\varepsilon_2(\omega)$ and $\alpha(\omega)$.

A significant parameter that illustrates the transport of charge carriers to optical frequencies is optical conductivity σ(ω) [47]. Figure 7(f) shows the simulated graphs of σ(ω) for Na_2CuMX_6 double perovskites. The values of σ(ω) exhibit a value of zero within the frequency range beyond the optical

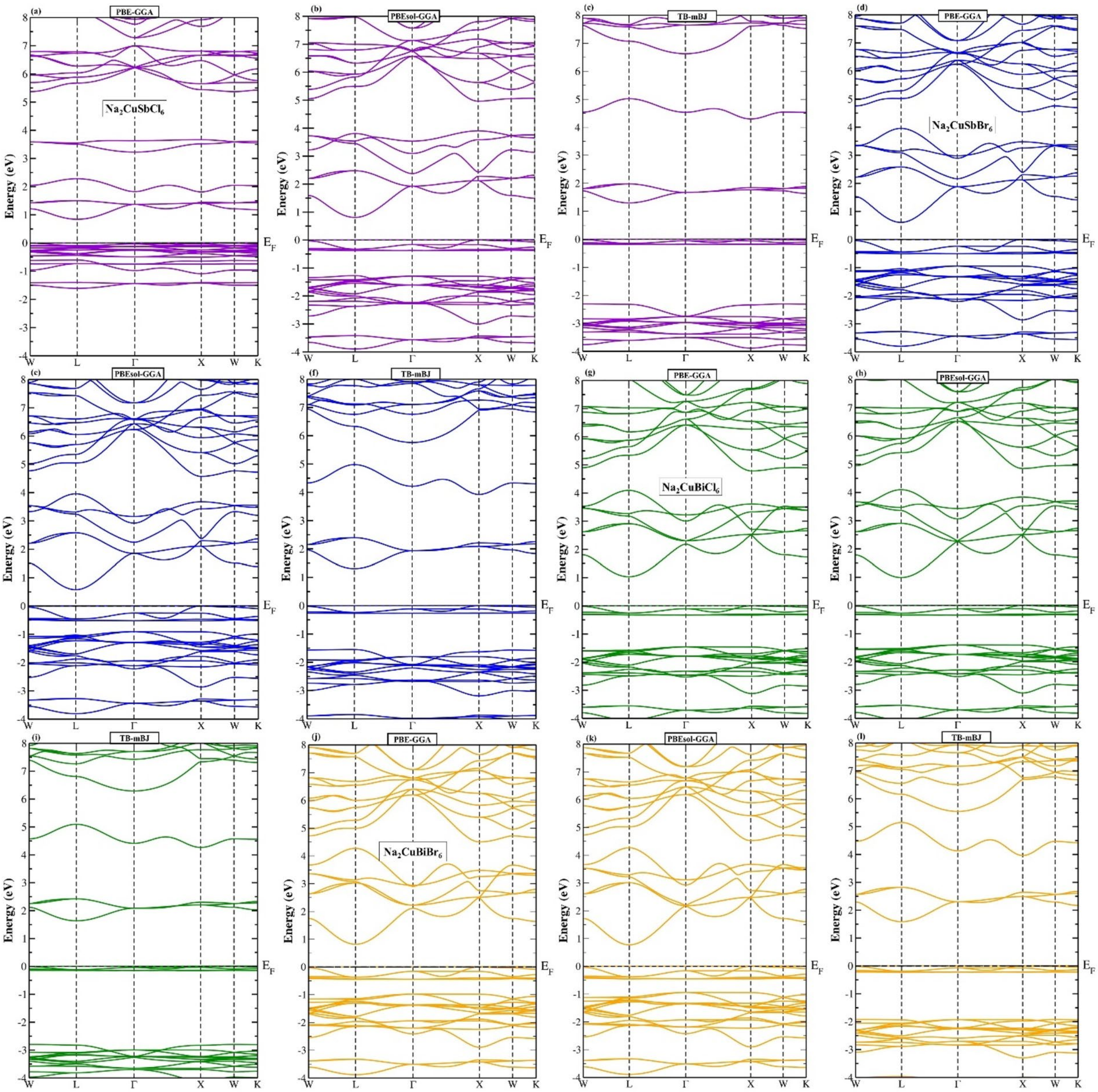

Figure 4: Comparison between the band structures calculated utilizing PBE-GGA, PBEsol-GGA, and mBJ for (a–c) $Na_2CuSbCl_6$ (d–f) $Na_2CuSbBr_6$ (g–i) $Na_2CuBiCl_6$ (j–l) $Na_2CuBiBr_6$.

band gap. The charge carriers are excited by the optical photon, possessing energy equivalent to the optical band gap. $Na_2CuSbBr_6$ exhibits the highest optical conductivity of 1100 Ω^{-1} cm^{-1} at the energy of 2.3 eV, followed by $Na_2CuBiBr_6$, having optical conductivity of 970.8 Ω^{-1} cm^{-1}.

Reflectivity is the ratio of the intensity of radiation striking a surface to the intensity of light reflecting [59]. In Fig. 7(g), the pattern of R(ω) is shown. The static reflectance values R(0) calculated for Na_2CuMX_6 (M = Sb, Bi, and X = Cl, Br) were less than 10%. The values for the R(ω) in the visible range are less than 20%. This indicates that all of the investigated double perovskites, Na_2CuMX_6, can absorb the greatest amount of visible photons. So, we recommend these materials for use in solar cell applications. Moreover, some of the light energy is lost through dispersion and many other losses. As a result, A graph of the optical energy loss L(ω) has been depicted in Fig. 7(h), demonstrating extremely low for the $Na_2CuSbBr_6$ and $Na_2CuBiBr_6$ double perovskites. These materials absorb the majority of the incident energy. It has been determined that all investigated perovskite materials, especially $Na_2CuSbBr_6$ and $Na_2CuBiBr_6$, are significant for solar cells based on a detailed investigation of the optical response of these materials.

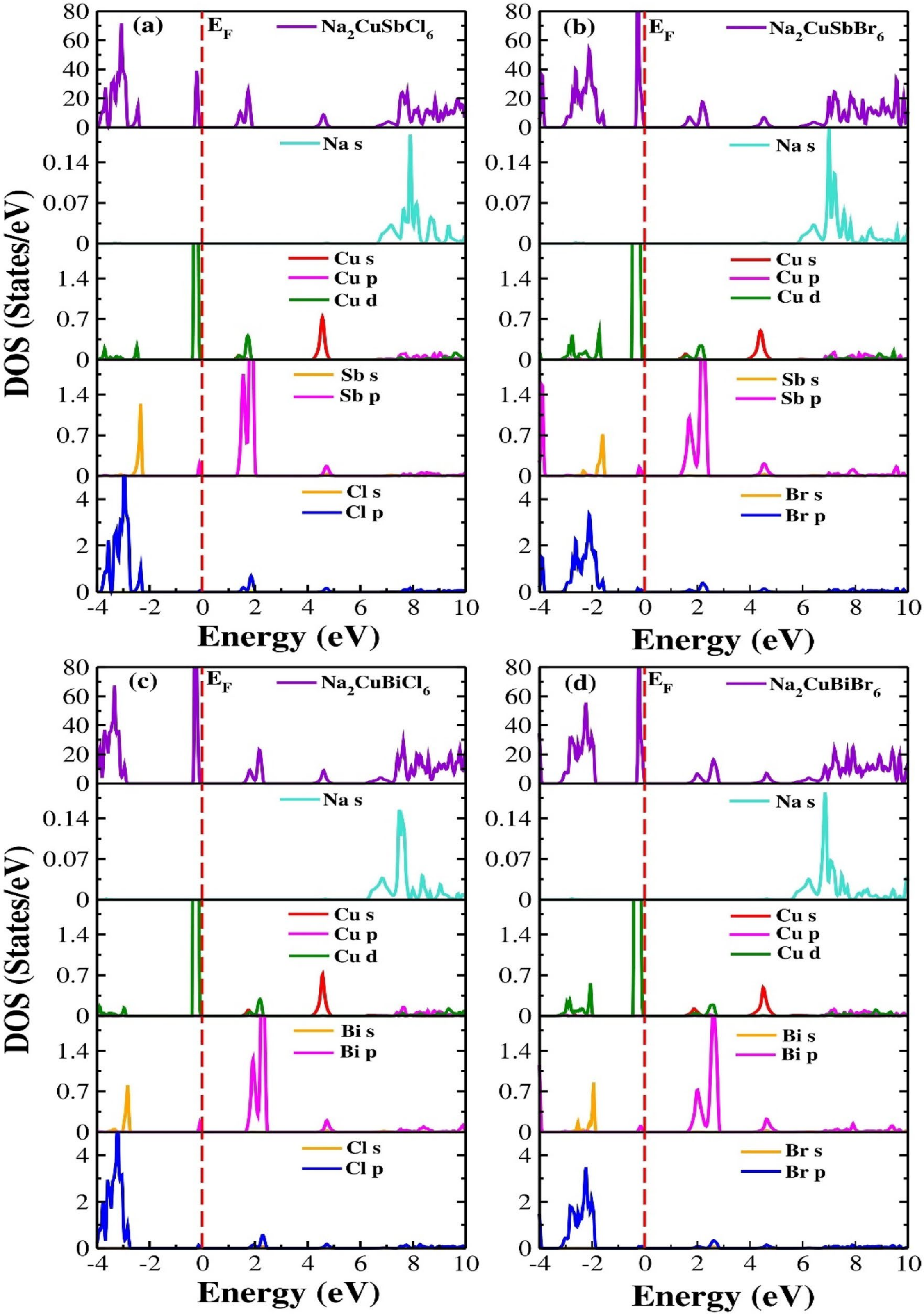

Figure 5: DOS plots of materials and individual components Na, Cu, Sb/Br, and Cl/Br of (a) $Na_2CuSbCl_6$ (b) $Na_2CuSbBr_6$ (c) $Na_2CuBiCl_6$ (d) $Na_2CuBiBr_6$.

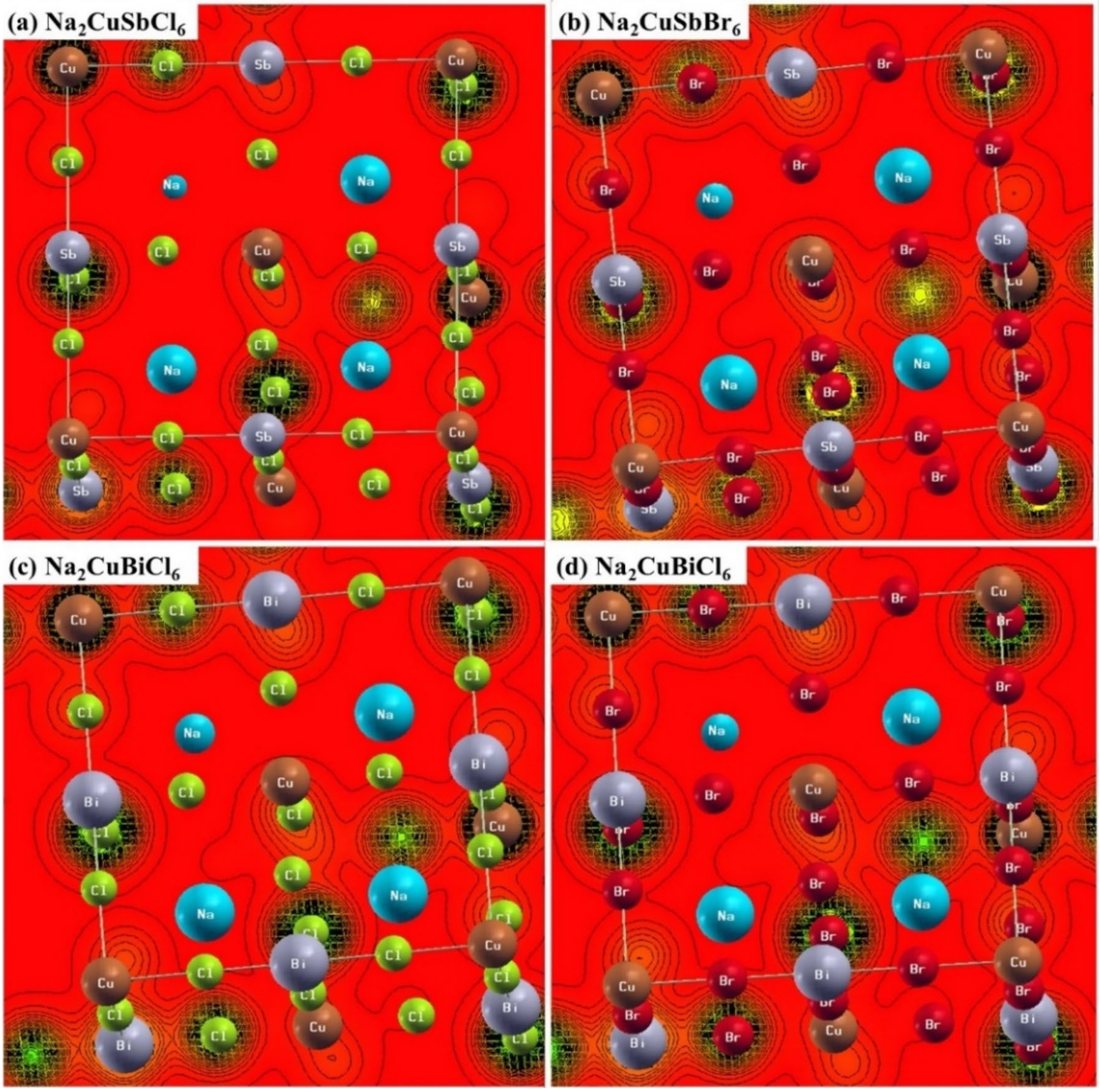

Figure 6: The electronic charge density (ECD) within the (110) plane for (a) $Na_2CuSbCl_6$ (b) $Na_2CuSbBr_6$ (c) $Na_2CuBiCl_6$ (d) $Na_2CuBiBr_6$.

Transport properties

Utilizing thermoelectric materials, waste heat may be converted into valuable electrical energy. Perovskites are especially advantageous for this purpose because of their accessibility, affordability, excellent electrical conductivity, and environmental friendliness [60]. The essential transport characteristics were computed against temperature in the 200–800 K range, by using the WIEN2k output files as the input files in the BoltzTraP code, with the assumption of a constant relaxation time (τ) [61, 62]. In the BoltzTraP code, its value is maintained constant at 10^{-14}. The perturbing duration of lattice vibration is measured by this relaxation time [63]. The figure of merit $ZT = \frac{S^2 \sigma T}{\kappa}$, where "S" stands for the Seebeck coefficient, which is determined by the potential gradient between different metals, " σ" for electrical conductivity, which controls carrier movement, and "κ" for thermal conductivity, which is determined by lattice vibration, is used to analyze the efficiency of thermoelectric materials. For optimal performance, the S and must be as high as possible, and the k as low as possible [63–65]. The computed output data obtained using the BoltzTraP code is plotted in Fig. 8.

The Seebeck effect is the electric potential that arises due to a temperature differential in different electrical conductors or semiconductors. The measured value of the Seebeck coefficient, as mentioned in Fig. 8(a) dropped exponentially with temperature for all compounds, peaking at 200 K with a value of 226 μV/K for $Na_2CuSbCl_6$, 239 μV/K for $Na_2CuSbBr_6$, 220 μV/K for $Na_2CuBiCl_6$, and 235 μV/K for $Na_2CuBiBr_6$. The

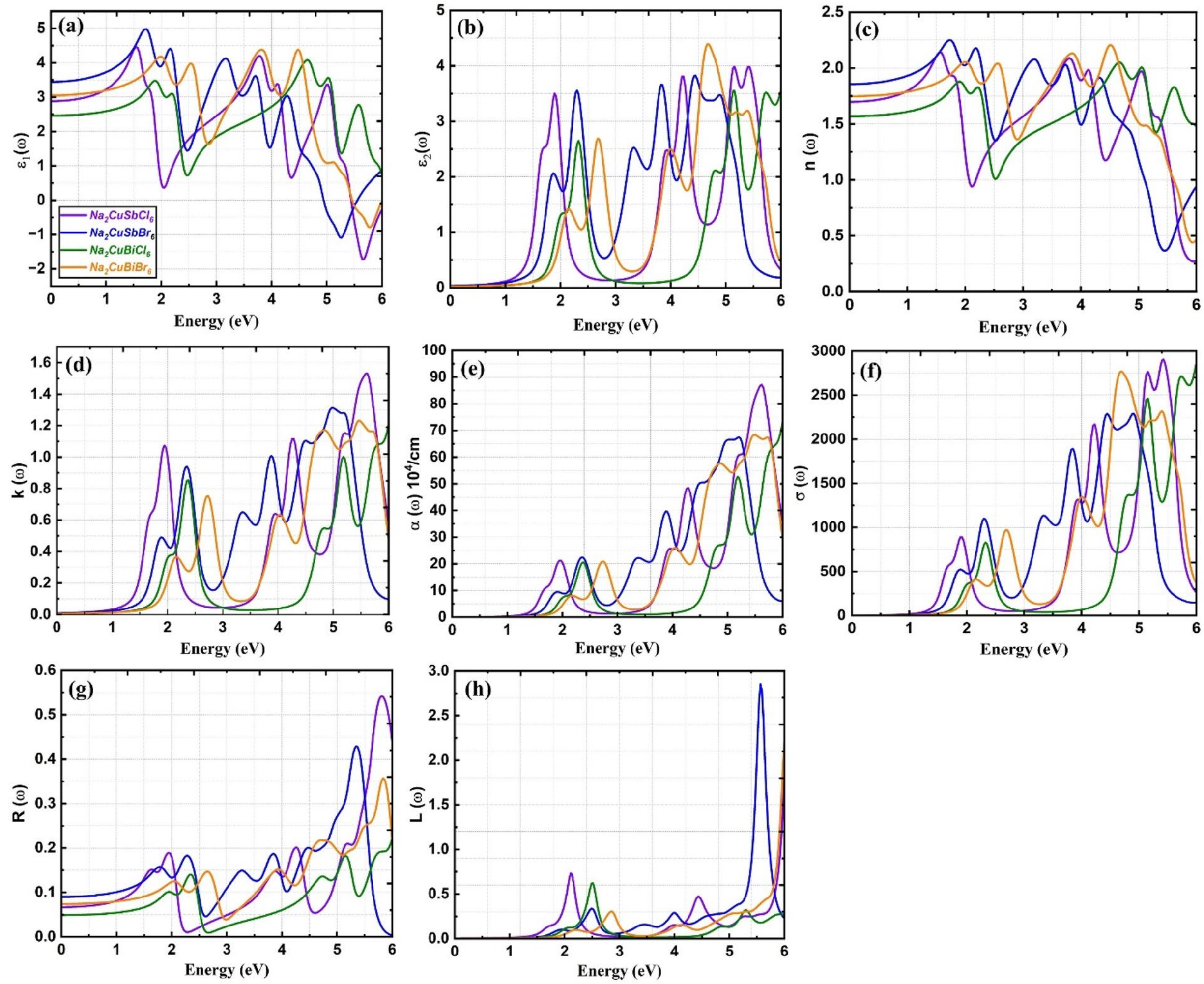

Figure 7: Optical parameters (a) real part of dielectric function (b) imaginary part of dielectric function (c) refractive index (d) extinction coefficient (e) absorption coefficient (f) optical conductivity (g) reflectivity (h) energy loss for Na$_2$CuMX$_6$ (M = Sb, Bi, and X = Cl, Br).

positive "S" values of the compounds show their p-type nature, which makes them active thermoelectric materialsThe Seebeck coefficient was found to be maximum at 300 K (room temperature) for Na$_2$CuSbBr$_6$ and Na$_2$CuBiBr$_6$.

The electrical conductivity (σ) enables us to understand how charge carriers and electric current relate to one another in materials. Electrical conductivity is highly desirable in a thermoelectric material since it lessens the Joule-heating impact [63]. The temperature-dependent σ in the 200–800 K range is shown in Fig. 8(b), and it rises linearly as the temperature rises. The calculated values of σ for Na$_2$CuSbCl$_6$, Na$_2$CuSbBr$_6$, Na2CuBiCl$_6$, and Na$_2$CuBiBr$_6$ at room temperature are 1.96×10^{18}, 2.15×10^{18}, 1.81×10^{18}, and 2.13×10^{18} Ω^{-1} m^{-1} s^{-1}, respectively. This indicates that electrical conductivity has larger values for Na$_2$CuSbBr$_6$ and Na$_2$CuBiBr$_6$.

Electrons and lattice vibration both contribute to thermal conductivity (κ_e and κ_{ph}) [66, 67]. In our calculations, we didn't take into account the effect of phonons caused by the very low thermal conductivity of the lattice in double perovskites, as reported for Cs2PtI6 [68], as well as complicated calculations and the limitations of the BoltzTraP code [46]. As a result, Fig. 8(c) shows a graph of the computed κ_e for the investigated double perovskites. Graph observation of κ_e assures identical behavior to that of σ as the room temperature values of Br-based Na$_2$CuSbBr$_6$ and Na$_2$CuBiBr$_6$ are higher than Cl-based compounds. The ratio κ_e /σ has been determined for the investigation of efficiency and confirms that s is 10^5 times larger than κ_e, making them highly important materials for thermoelectric generators [69].

The power factor (PF = S^{2}σ) is a fundamental factor to ensure thermoelectric material utilization for potential applications. Figure 8(d) plots the temperature-dependent power factor for all compounds. The PF values at room temperature (300 K) are 8.9×10^{10}, 10.8×10^{10}, 8.0×10^{10}, and 10.6×10^{10} W/mK^{2}s for Na$_2$CuSbCl$_6$, Na$_2$CuSbBr$_6$, Na$_2$CuBiCl$_6$, and Na$_2$CuBiBr$_6$, respectively. At higher temperatures (800 K), these values decrease to 3.1×10^{10}, 9.0×10^{10},

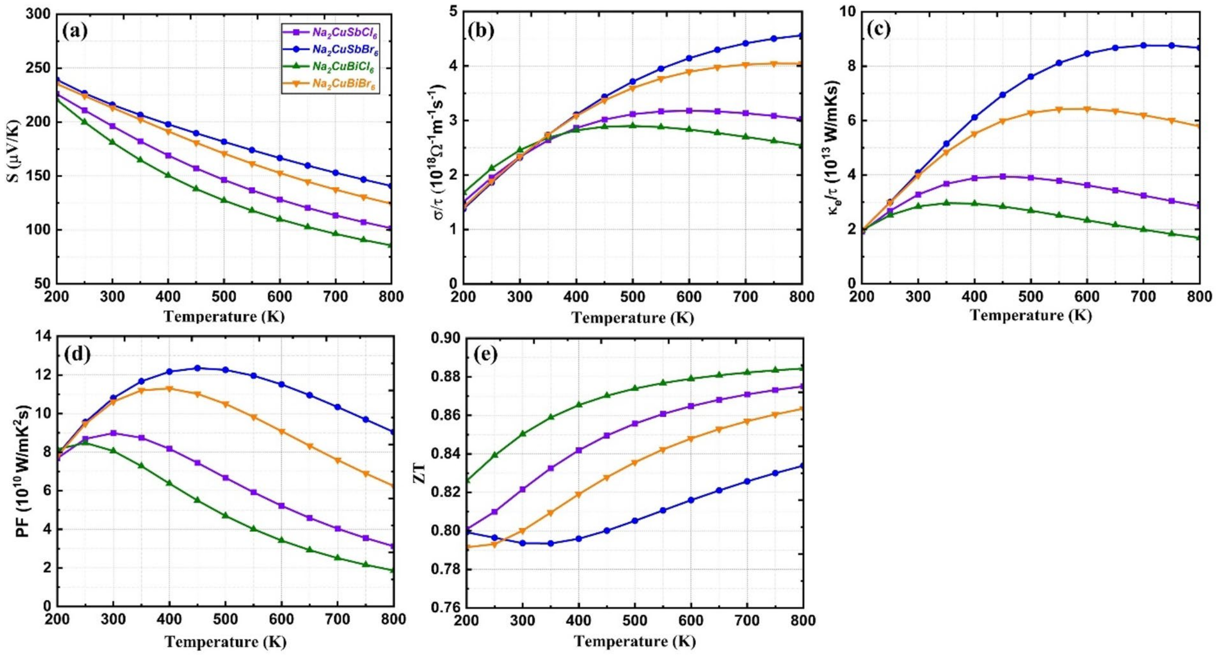

Figure 8: Temperature-dependent thermoelectric parameters (a) Seebeck coefficient (b) electrical conductivity (c) thermal conductivity (d) power factor (e) figure of merit for Na_2CuMX_6 (M = Sb, Bi, and X = Cl, Br).

1.86×10^{10} and 6.2×10^{10} W/mK^{2}s, respectively. The Plots depict the rising PF behavior with temperature and illustrate these materials as suitable for thermoelectricity.

The figure of merit $ZT = \frac{S^2\sigma T}{\kappa}$ defines the most effective thermoelectric properties of any material. The relation for the figure of merit reveals the value of ZT varies directly with the Seebeck coefficient. A material that is ideal for thermoelectric use must have a ZT value equal to one that provides a better energy conversion efficiency (> 25%) at the ideal operating temperature [58]. Figure 8(e) shows that the highest ZT values found to be 0.82, 0.79, 0.85, and 0.81 for $Na_2CuSbCl_6$, $Na_2CuSbBr_6$, $Na_2CuBiCl_6$, and $Na_2CuBiBr_6$, respectively, at room temperature were increased to 0.87, 0.83, 0.88, and 0.86, respectively, with an increase in temperature up to 800 K. This shows that all materials under study are efficient thermoelectrics. These results suggest that all investigated compounds have remarkable thermoelectric characteristics, especially $Na_2CuBiCl_6$, which has slightly higher ZT values, making them suitable for potential use in thermoelectric devices.

Conclusion

The computational investigation involved the utilization of the WIEN2k software package to analyze the elastic, structural, optoelectronic, and transport properties of Na_2CuMX_6 (M = Sb, Bi, and X = Cl, Br) double perovskites. The double perovskites under investigation exhibit stable cubic structures. The indirect band gap when considering the symmetry points (L–X) indicates that all the materials possess semiconductor properties. The brittle or ductile nature, anisotropy, and elastic stability of the Na_2CuMX_6 (M = Sb, Bi, and X = Cl, Br) double perovskites are evident from their mechanical properties. All the materials exhibit brittle nature except $Na_2CuSbCl_6$, which was ductile. The calculated band gap (E_g) for $Na_2CuSbCl_6$, $Na_2CuSbBr_6$, $Na_2CuBiCl_6$, and $Na_2CuBiBr_6$ double perovskites were determined to be 1.26 eV, 1.3 eV, 1.62 eV, and 1.57 eV using the TB-mBJ functional. The optical properties estimated within the range of energies of 0–6 eV possess the potential to be utilized in optoelectronic and photovoltaic devices due to their anticipated maximum optical conductivity, lower reflectivity (less than 20%), and ability to absorb incident photons within the visible region. Moreover, these materials exhibit a significantly high “S” and “ZT” (figure of merit), indicating their potential for thermoelectric applications. The results reveal that the perovskites under investigation have promising characteristics for use in solar and thermoelectric applications.

Computational details

To examine the physical characteristics of the Na_2CuMX_6 (M = Sb, Bi, and X = Cl, Br) materials, we conducted Density Functional Theory (DFT) calculations using the full-potential linearized augmented plane wave (FP-LAPW) technique included in the WIEN2k interface [70, 71]. The exchange–correlation functional of Perdew–Burke–Ernzerhof generalized gradient approximation (PBE-GGA) was used to optimize the structures of all the compounds in the cubic phase [72]. The structural characteristics are obtained accurately using the PBE-GGA. The Generalized gradient approximation (GGA) is used to determine electronic properties both with and without the Tran and Blaha modified Becke and Johnson potential (TB-mBJ). The GGA approximation underestimating the E_g was compensated by employing the TB-mBJ functional [72–74]. The TB-mBJ has been utilized to eliminate the underestimation problem of band gap, which was identified by the PBE-GGA and PBEsol-GGA functionals [75]. The wave functions were produced using a foundation of plane waves with the value of the product of the cut-off reciprocal lattice vector and $R_{min}MT$ was adjusted to 10, where $R_{min}MT$ indicates the minimum muffin-tin sphere radius (RMT). The RMT was set as high as possible for atoms i.e. $R_{MT}^{Na} = 2.0, R_{MT}^{Cu} = 1.5, R_{MT}^{M} = 1.9, \text{and} R_{MT}^{X} = 2.0$ to prevent spheres from overlapping. To ensure convergence, we also sampled the Brillion Zone (BZ) utilizing a dense mesh of 100 k points. Energy and charge convergence between consecutive cycles converged to a value of 0.0001 Ry and 0.0001 e, respectively, which improved results. The optical characteristics were calculated using the OPTIC package within the WIEN2k framework [76, 77]. The thermoelectric characteristics were calculated using the BoltzTraP algorithm using an estimate of constant relaxation time (τ) [61, 78, 79].

Acknowledgments

The authors acknowledge the Centre for Advanced Studies in Physics (CASP), Government College University, Lahore, Pakistan, by offering the characterization facilities, computer facilities, and software package essential for this work.

Authors contributions

The entire team of authors worked on the article. GM gave an idea about the manuscript and supervised the whole work. AA and MU performed the DFT calculations and wrote the whole manuscript in collaboration. AU prepared figures and tables for the manuscript.

Data availability

The corresponding author will provide the data generated during the study upon a reasonable request.

Declarations

Conflict of interest There are no competing interests among the authors in publishing this work.

Ethical approval

Not applicable.

References

1. W. Zhang, G.E. Eperon, H.J. Snaith, Metal halide perovskites for energy applications. Nat. Energy **1**(6), 1–8 (2016)
2. W.J. Yin, T. Shi, Y. Yan, Unique properties of halide perovskites as possible origins of the superior solar cell performance. Adv. Mater. **26**(27), 4653–4658 (2014)
3. F. Giustino, H.J. Snaith, Toward lead-free perovskite solar cells. ACS Energy Lett. **1**(6), 1233–1240 (2016)
4. P.V. Kamat, J. Bisquert, J. Buriak, Lead-free perovskite solar cells. ACS Energy Lett. **2**(4), 904–905 (2017)
5. Q. Fan, G.V. Biesold-McGee, J. Ma, Q. Xu, S. Pan, J. Peng, Z. Lin, Lead-free halide perovskite nanocrystals: crystal structures, synthesis, stabilities, and optical properties. Angew. Chem. Int. Ed. **59**(3), 1030–1046 (2020)
6. J. Sun, J. Yang, J.I. Lee, J.H. Cho, M.S. Kang, Lead-free perovskite nanocrystals for light-emitting devices. J. Phys. Chem. Lett. **9**(7), 1573–1583 (2018)
7. B. Yang, K. Han, Charge-carrier dynamics of lead-free halide perovskite nanocrystals. Acc. Chem. Res. **52**(11), 3188–3198 (2019)
8. B. Yang, X. Mao, F. Hong, W. Meng, Y. Tang, X. Xia et al., Lead-free direct band gap double-perovskite nanocrystals with bright dual-color emission. J. Am. Chem. Soc. **140**(49), 17001–17006 (2018)
9. T. Cai, W. Shi, S. Hwang, K. Kobbekaduwa, Y. Nagaoka, H. Yang et al., Lead-free Cs4CuSb2Cl12 layered double perovskite nanocrystals. J. Am. Chem. Soc. **142**(27), 11927–11936 (2020)
10. H. Yang, T. Cai, E. Liu, K. Hills-Kimball, J. Gao, O. Chen, Nano Res. **13**, 282 (2020)
11. L. Zhang, K. Wang, B. Zou, Bismuth halide perovskite-like materials: current opportunities and challenges. Chemsuschem **12**(8), 1612–1630 (2019)
12. M.Z. Rahaman, A.M.A. Hossain, Effect of metal doping on the visible light absorption, electronic structure and mechanical properties of non-toxic metal halide CsGeCl 3. RSC Adv. **8**(58), 33010–33018 (2018)
13. W. Shi, T. Cai, Z. Wang, O. Chen, The effects of monovalent metal cations on the crystal and electronic structures of Cs2MBiCl6 (M= Ag, Cu, Na, K, Rb, and Cs) perovskites. J. Chem. Phys. (2020). https://doi.org/10.1063/5.0021238
14. S. Al-Qaisi, M. Mushtaq, S. Alomairy, T.V. Vu, H. Rached, B.U. Haq et al., First-principles investigations of Na2CuMCl6 (M= Bi, Sb) double perovskite semiconductors: materials for green technology. Mater. Sci. Semicond. Process. **150**, 106947 (2022)
15. S. Kumari, P.K. Kamlesh, L. Kumari, S. Kumar, S. Kumari, R. Singh et al., Progress in theoretical study of lead-free halide double perovskite Na2AgSbX6 (X= F, Cl, Br, and I) thermoelectric materials. J. Mol. Model. **29**(6), 195 (2023)
16. P.R. Varadwaj, A 2 AgCrCl 6 (A= Li, Na, K, Rb, Cs) halide double perovskites: a transition metal-based semiconducting material

series with appreciable optical characteristics. Phys. Chem. Chem. Phys. **22**(42), 24337–24350 (2020)

17. P.D. Sreedevi, P. Ravindran, R. Vidya, First principles prediction of the ground state crystal structures of antiperovskite compounds A3PN (A= Be, Mg, Ca, Sr, Ba and Zn). Mater. Today: Proc. **8**, 294–300 (2019)
18. W.J. Yin, J.H. Yang, J. Kang, Y. Yan, S.H. Wei, Halide perovskite materials for solar cells: a theoretical review. J. Mater. Chem. A **3**(17), 8926–8942 (2015)
19. T.Y. Tang, Y.L. Tang, Physical and optoelectronic properties of double halide perovskites A2CuSbX6 (A= Cs, Rb, K; X= Cl, Br, I) based on first principles calculations. Chem. Phys. **570**, 111897 (2023)
20. M. Asghar, M. Zanib, M.A. Khan, S. Niaz, N.A. Noor, A. Dahshan, Tuning of the bandgap of Rb2ScAgX6 (X= Cl, Br, I) double perovskites through halide ion replacement for solar cell applications. Mater. Sci. Semicond. Process. **148**, 106819 (2022)
21. D. Behera, S.K. Mukherjee, First-principles calculations to investigate structural, optoelectronics and thermoelectric properties of lead free Cs2GeSnX6 (X= Cl, Br). Mater. Sci. Eng. B **292**, 116421 (2023)
22. C. Vorwerk, C. Hartmann, C. Cocchi, G. Sadoughi, S.N. Habisreutinger, R. Félix et al., Exciton-dominated core-level absorption spectra of hybrid organic–inorganic lead halide perovskites. J. Phys. Chem. Lett. **9**(8), 1852–1858 (2018)
23. R.A. Jishi, O.B. Ta, A.A. Sharif, Modeling of lead halide perovskites for photovoltaic applications. J. Phys. Chem. C **118**(49), 28344–28349 (2014)
24. E.T. McClure, M.R. Ball, W. Windl, P.M. Woodward, Cs2AgBiX6 (X= Br, Cl): new visible light absorbing, lead-free halide perovskite semiconductors. Chem. Mater. **28**(5), 1348–1354 (2016)
25. M. Irfan, G. Murtaza, N. Muhammad, S. Tahir, H.H. Raza, B. Sabir et al., Experimental and theoretical studies of structural, electronic and magnetic properties of RE2NiCrO6 (RE = Ce, Pr and Nd) double perovskites. Physica E: Low-dimensional Syst. Nanostruct. **148**, 115635 (2023)
26. A.E. Fedorovskiy, N.A. Drigo, M.K. Nazeeruddin, The role of Goldschmidt's tolerance factor in the formation of A2BX6 double halide perovskites and its optimal range. Small Methods **4**(5), 1900426 (2020)
27. R. Ullah, M.A. Ali, A. Khan, R.A. Alshgari, M.S.S. Mushab, A. Samad, Effect of cation exchange on structural, electronic, magnetic and transport properties of Ba2MReO6 (M= In, Gd). J. Magn. Magn. Mater. **546**, 168816 (2022)
28. D. Behera, S.K. Mukherjee, Optoelectronics and transport phenomena in Rb2InBiX6 (X= Cl, Br) compounds for renewable energy applications: a DFT insight. Chemistry **4**(3), 1044–1059 (2022)
29. M.A. Blanco, E. Francisco, V. Luana, GIBBS: isothermal-isobaric thermodynamics of solids from energy curves using a quasi-harmonic Debye model. Comput. Phys. Commun. **158**(1), 57–72 (2004)
30. V.G. Tyuterev, N. Vast, Murnaghan's equation of state for the electronic ground state energy. Comput. Mater. Sci. **38**(2), 350–353 (2006)
31. F. Mouhat, F.X. Coudert, Necessary and sufficient elastic stability conditions in various crystal systems. Phys. Rev. B **90**(22), 224104 (2014)
32. N. Erum, J. Ahmad, M.A. Iqbal, M. Ramzan, DFT insights of mechanical, optoelectronic and thermoelectric properties for Cs2ScTlX6 (X= Cl, Br, I) double perovskites. Opt. Quant. Electron. **55**(4), 337 (2023)
33. M.A. Ali, M.A. Hossain, M.A. Rayhan, M.M. Hossain, M.M. Uddin, M. Roknuzzaman et al., First-principles study of elastic, electronic, optical and thermoelectric properties of newly synthesized K2Cu2GeS4 chalcogenide. J. Alloys Compound. **781**, 37–46 (2019)
34. T. Van Mourik, R.J. Gdanitz, A critical note on density functional theory studies on rare-gas dimers. J. Chem. Phys. **116**(22), 9620–9623 (2002)
35. S.F. Pugh, XCII. Relations between the elastic moduli and the plastic properties of polycrystalline pure metals. The London, Edinburgh, and Dublin Philosophical Magazine J. Sci. **45**(367), 823–843 (1954)
36. D. Behera, B. Mohammed, S. Taieb, B. Mokhtar, S. Al-Qaisi, S.K. Mukherjee, First-principle investigations on optoelectronics and thermoelectric properties of lead-free Rb2InSbX6 (X = Cl, Br) double perovskites: for renewable energy applications. Euro. Phys. J. Plus **138**(6), 520 (2023)
37. P. Haas, F. Tran, P. Blaha, Calculation of the lattice constant of solids with semilocal functionals. Phys. Rev. B **79**(8), 085104 (2009)
38. F. Wooten, *Optical properties of solids* (Academic Press, Cambridge, 1972)
39. N. Erum, M.A. Iqbal, First principles investigation of fluorine based strontium series of perovskites. Commun. Theor. Phys. **66**(5), 571 (2016)
40. I. Waller, Dynamical theory of crystal lattices by M. Born and K. Huang. Acta Crystallogr. A **9**(10), 837–838 (1956)
41. O.L. Anderson, A simplified method for calculating the Debye temperature from elastic constants. J. Phys. Chem. Solids **24**(7), 909–917 (1963)
42. A. Maachou, H. Aboura, B. Amrani, R. Khenata, S.B. Omran, D. Varshney, Structural stabilities, elastic and thermodynamic properties of scandium chalcogenides via first-principles calculations. Comput. Mater. Sci. **50**(11), 3123–3130 (2011)
43. R. Gaillac, P. Pullumbi, F.X. Coudert, ELATE: an open-source online application for analysis and visualization of elastic tensors. J. Phys. Condens. Matter **28**(27), 275201 (2016)
44. M.A.H. Shah, M. Nuruzzaman, A. Hossain, M. Jubair, M.A.K. Zilani, A DFT insight into structural, mechanical,

elasto-acoustic, and anisotropic properties of AePdH3 (Ae = Ca, Sr, Ba) perovskites under pressure. Comput. Condens. Matter **34**, e00774 (2023)

45. N. Rahman, A. Rauf, M. Husain, N. Sfina, V. Tirth, M. Sohail et al., Probing the physical properties of M2LiCeF 6 (M= Rb and Cs) double perovskite compounds for prospective high-energy applications employing the DFT framework. RSC Adv. **13**(23), 15457–15466 (2023)
46. A. Mera, T. Zelai, S.A. Rouf, N.A. Kattan, Q. Mahmood, First-principles calculations to investigate mechanical, thermoelectric and optical performance of inorganic double perovskites Rb2AgAlZ6 (Z= Br, I) for energy harvesting. J. Market. Res. **24**, 5588–5597 (2023)
47. M.A. Ali, A.A. Alothman, M. Mushab, A. Khan, M. Faizan, DFT insight into structural, electronic, optical and thermoelectric properties of eco-friendly double perovskites Rb2GeSnX6 (X = Cl, Br) for green energy generation. J. Inorg. Organomet. Polym. Mater. (2023). https://doi.org/10.1007/s10904-023-02777-8
48. N. Alaal, I.S. Roqan, Tuning the electronic properties of hexagonal two-dimensional GaN monolayers via doping for enhanced optoelectronic applications. ACS Appl. Nano Mater. **2**(1), 202–213 (2018)
49. S. Tariq, M.I. Jamil, A. Sharif, S.M. Ramay, H. Ahmad, N. Ul Qamar, B. Tahir, Exploring structural, electronic and thermo-elastic properties of metallic AMoO 3 (A= Pb, Ba, Sr) molybdates. Appl. Phys. A **124**, 1–8 (2018)
50. Q. Mahmood, G. Nazir, S. Bouzgarrou, A.I. Aljameel, A. Rehman, H. Albalawi et al., Study of new lead-free double perovskites halides Tl2TiX6 (X= Cl, Br, I) for solar cells and renewable energy devices. J. Solid State Chem. **308**, 122887 (2022)
51. T. Zelai, S.A. Rouf, Q. Mahmood, S. Bouzgarrou, M.A. Amin, A.I. Aljameel et al., First-principles study of lead-free double perovskites Ga2PdX6 (X= Cl, Br, and I) for solar cells and renewable energy. J. Mater. Res. Technol. **16**, 631–639 (2022)
52. H. Belhadj, M. Ameri, B. Abbar, N. Moulay, A.Z. Bouyakoub, O. Arbouche et al., Optical properties of (Pb1-xMnxS) 1-yFey materials from first-principles calculations. Chin. J. Phys. **55**(3), 1032–1043 (2017)
53. Y. Al-Douri, M. Ameri, A. Bouhemadou, K.M. Batoo, First-principles calculations to investigate the refractive index and optical dielectric constant of Na3SbX4 (X= S, Se) ternary chalcogenides. Physica Status Solidi (b) **256**(11), 1900131 (2019)
54. S.S. Essaoud, A. Bouhemadou, M.E. Ketfi, D. Allali, S. Bin-Omran, Structural parameters, electronic structure and linear optical functions of LuXCo2Sb2 (X= V, Nb and Ta) double half Heusler alloys. Physica B **657**, 414809 (2023)
55. M.A. Ali, R.A. Alshgari, A.A. Awadh Bahajjaj, M. Sillanpää, The study of new double perovskites K2AgAsX6 (X= Cl, Br) for energy-based applications. J. Taibah Univ. Sci. **17**(1), 2170680 (2023)
56. U. Duman, M. Aycibin, Ö.F. Özdemir, The electronic, structural, and optical properties of $CaNb_2O_6$ compound: theoretical study. Physica Status Solidi (b) **258**(12), 2100416 (2021)
57. T. Seddik, D. Behera, M. Batouche, W. Ouerghui, H.B. Abdallah, R.K. Sarkar et al., Electronic properties, linear and nonlinear performance of KAg Ch (Ch= S, Se) compounds: a first-principles study. Crystals **13**(5), 726 (2023)
58. D. Behera, M. Manzoor, M.W. Iqbal, S. Lakra, S.K. Mukherjee, Revealing excellent electronic, optical, and thermoelectric behavior of Eu based EuAg2Y2 (Y= S/Se): for solar cell applications. Comput. Condensed Matter **32**, e00723 (2022)
59. Y. Cai, M. Faizan, X. Shen, A.M. Mebed, T.A. Alrebdi, X. He, NaBeAs and NaBeSb: novel ternary pnictides with enhanced thermoelectric performance. J. Phys. Chem. C **127**(4), 1733–1743 (2023)
60. G. Murtaza, A.A. AlObaid, T.I. Al-Muhimeed, S. Al-Qaisi, A. Rehman, H.H. Hegazy et al., Tailoring of band gap to tune the optical and thermoelectric properties of Sr1-xBaxSnO3 stannates for clean energy; probed by DFT. Chem. Phys. **551**, 111322 (2021)
61. G.K. Madsen, D.J. Singh, BoltzTraP. A code for calculating band-structure dependent quantities. Comput. Phys. Commun. **175**(1), 67–71 (2006)
62. T.J. Scheidemantel, C. Ambrosch-Draxl, T. Thonhauser, J.V. Badding, J.O. Sofo, Transport coefficients from first-principles calculations. Phys. Rev. B **68**(12), 125210 (2003)
63. Q. Mahmood, T. Zelai, T. Usman, S. Al-Qaisi, M. Morsi, H. Albalawi et al., First-principles study of lead-free double perovskites K2Pt (Cl/Br) 6 for optoelectronic and renewable energy applications. J. Solid State Chem. **301**, 122294 (2021)
64. Q. Mahmood, M.H. Alhossainy, M.S. Rashid, T.H. Flemban, H. Althib, T. Alshahrani et al., First-principles study of lead-free double perovskites Rb2TeX6 (X= Cl, Br, and I) for solar cells and renewable energy. Mater. Sci. Eng. B **266**, 115064 (2021)
65. T.H. Flemban, V. Singaravelu, A.A.S. Devi, I.S. Roqan, Homogeneous vertical ZnO nanorod arrays with high conductivity on an in situ Gd nanolayer. RSC Adv. **5**(115), 94670–94678 (2015)
66. A.H. Reshak, S.A. Khan, S. Auluck, Thermoelectric properties of a single graphene sheet and its derivatives. J. Mater. Chem. C **2**(13), 2346–2352 (2014)
67. A.H. Reshak, S. Auluck, Thermoelectric properties of Nowotny-Juza NaZnX (X= P, As and Sb) compounds. Comput. Mater. Sci. **96**, 90–95 (2015)
68. M. Sajjad, Q. Mahmood, N. Singh, J.A. Larsson, Ultralow lattice thermal conductivity in double perovskite Cs2PtI6: a promising thermoelectric material. ACS Appl. Energy Mater. **3**(11), 11293–11299 (2020)
69. M. Sajjad, N. Singh, S. Sattar, S. De Wolf, U. Schwingenschlögl, Ultralow lattice thermal conductivity and thermoelectric

properties of monolayer Tl2O. ACS Appl. Energy Mater. **2**(5), 3004–3008 (2019)

70. P. Blaha, K. Schwarz, F. Tran, R. Laskowski, G.K. Madsen, L.D. Marks, WIEN2k: an APW+ lo program for calculating the properties of solids. J. Chem. Phys. (2020). https://doi.org/10.1063/1.5143061
71. P. Hohenberg, W. Kohn, Inhomogeneous electron gas. Phys. Rev. **136**(3B), B864 (1964)
72. J.P. Perdew, K. Burke, M. Ernzerhof, Generalized gradient approximation made simple. Phys. Rev. Lett. **77**(18), 3865 (1996)
73. D. Koller, F. Tran, P. Blaha, Merits and limits of the modified Becke-Johnson exchange potential. Phys. Rev. B **83**(19), 195134 (2011)
74. M.A. Ali, R. Ullah, S. Murad, S.A. Dar, A. Khan, G. Murtaza, A. Laref, Insight into pressure tunable structural, electronic and optical properties of [see pdf] via DFT calculations. Euro. Phys. J. Plus **135**(3), 309 (2020)
75. J.P. Perdew, A. Ruzsinszky, G.I. Csonka, O.A. Vydrov, G.E. Scuseria, L.A. Constantin et al., Restoring the density-gradient expansion for exchange in solids and surfaces. Phys. Rev. Lett. **100**(13), 136406 (2008)
76. M. Fox, Classical propagation. Opt. Prop. Solids **2**, 28–58 (2001)
77. I. Khan, I. Ahmad, B. Amin, G. Murtaza, Z. Ali, Bandgap engineering of Cd1− xSrxO. Physica B **406**(13), 2509–2514 (2011)
78. S. Alnujaim, A. Bouhemadou, M. Chegaar, A. Guechi, S. Bin-Omran, R. Khenata et al., Density functional theory screening of some fundamental physical properties of $Cs_2InSbCl_6$ and $Cs_2InBiCl_6$ double perovskites. Euro. Phys. J. B **95**(7), 114 (2022)
79. M.J. Alrahamneh, A.A. Mousa, J.M. Khalifeh, First principles study of the structural, electronic, magnetic and thermoelectric properties of Zr2RhAl. Physica B **552**, 227–235 (2019)